Case Studies in Thermal Engineering 13 (2019) 100379

Contents lists available at ScienceDirect

Case Studies in Thermal Engineering

journal homepage: www.elsevier.com/locate/csite

Prediction of heat transfer coefficient during quenching of large size forged blocks using modeling and experimental validation

Yassine Bouissa*, Davood Shahriari, Henri Champliaud, Mohammad Jahazi*

Mechanical Engineering Department, École de technologie supérieure, 1100, rue Notre-Dame Ouest, Montréal (QC), Canada, H3C 1K3

ARTICLE INFO

Keywords:
Heat transfer coefficient of steel quenching
large forged blocks
FEM simulation
Artificial Neural Network
TTT
Phase transformation

ABSTRACT

In this study, a new method is developed to predict an accurate convective heat transfer coefficient (HTC) during quenching of large size steel blocks, using a combination of 3D Finite Element (FEM) simulations and a progressive artificial neural network (ANN).

The HTC profile of the first inputs used for FEM simulations were acquired from the literature to calculate the cooling temperature profiles at specific locations. The training of the ANN was set up between HTCs and their corresponding FEM-calculated temperature. Experimental validation was carried out by instrumenting a large size forged steel block during the quench process. The experimental cooling curves were used for validation of the FEM simulation, as well as for the prediction of new HTCs by simulating the ANN. Results show that the proposed method provides progressively more accurate predictions than the existing ones reported in the literature.

A mean absolute percentage error (*MAPE*) of 1.47% was found between experimental and calculated cooling curves for the predicted HTC, further demonstrating a better prediction ability of the proposed method.

1. Introduction

Medium carbon low alloy steels are commonly used as die materials for plastic injection molds in the automotive industry [1]. The manufacturing process consists of ingots casting, open die forging, and finally, quench and temper operations [2]. Uniform hardness and grain size, along with a bainitic microstructure, are among the most important characteristics required by the industry for these steels. These characteristics are mostly dependent on the efficiency of quenching and temper operations [3,4]. Large size forging ingots must be produced in order to respond to demand by the automotive and trucking industries for the manufacture of large size plastic injection molded components [1]. However achieving a uniform hardness, microstructure and grain size through the thickness of a large size forged blocks during quenching and tempering is a very challenging task [4,5].

The challenge is mainly due to the formation of a significant thermal gradient between the surface and the center, associated with the large size of the block. Each point along the block is associated with a specific cooling profile, which in turn, is able to trigger a

Abbreviations: ANN, Artificial neural network; BP, Back-propagation; CCT, Continuous cooling transformation diagrams; FEM, Finite Element Method; HTC, Heat transfer coefficient; JMAK, Johnson-Mehl-Avrami-Kolmogorov model; MAPE, Mean absolute percentage error; Tansig, Hyperbolic tangent function; TTT, Time temperature transformation diagrams

* Corresponding authors.
E-mail addresses: yassine.bouissa@gmail.com (Y. Bouissa), mohammad.jahazi@etsmtl.ca (M. Jahazi).

https://doi.org/10.1016/j.csite.2018.100379
Received 28 September 2018; Received in revised form 14 December 2018; Accepted 16 December 2018
Available online 21 December 2018

Nomenclature

a	Activation function
B_s	Bainite transformation start temperature (in °C)
b_j, b_k	Bias of the neuron j , k
Cp	Specific heat (J.kg^{-1}. K^{-1})
ΔH^{φ}	Enthalpy of phase transformation (J.kg^{-1})
e_i, $e_i^{\,x}$	Absolute percentage error at time t_i
f	Volume fraction of each phase
f^{φ}	Volume fraction of the phase φ
h, HTC	Heat transfer coefficient (W.m^{-2}. K^{-1})
h_r	Heat transfer coefficient due to radiation (W.m^{-2}. K^{-1})
h_c	Heat transfer coefficient due to convection (W.m^{-2}. K^{-1})
$[HTC]_{k\times m}$	Heat transfer coefficient matrix with k lines and m columns
$HTC^{\,x}$	HTC column vector, where x is the column position of a matrix
$HTC^{\,ANN_p}$	HTC predicted by ANN, where p is the number of predictions
HTC_n	Normalized Heat transfer coefficient
L	Characteristic length (m)
M_s	Martensite transformation start temperature (in °C)
n, n_i	Exponent of JMAK equation at time t_i
P^{φ}	Thermo-physical property of the phase φ
Q	Internal heat source due to latent heat
R	Correlation coefficient
t	Time (s)
T	Temperature (in °C)
T_s	Temperature at the surface (in °C)
T_f	Temperature of fluid near to the surface (in °C)
$[T]_{i\times m}$	Temperature matrix with i lines and m columns
T_n	Normalized temperature
$T^{\,exp}$	Temperature measured by thermocouple (°C)
T^x	Temperature calculated by FEM, where x is the column position of a matrix
τ_i	Time step (s)
t_i^*	Fictitious time (s)
u_j	Output value of the neuron j
w_{ji}, w_{kj}	weight matrices

Greek symbols

α	Constant of Marburger equation
Ω	Volume domain used for simulation
Γ	Surface domain used for simulation
σ	Stefan-Boltzmann constant, $\sigma = 5.670367 \times 10^{-8}$ W.m^{-2}. K^{-4}
θ, θ_i	Constant of JMAK model,
φ	Denotes the present phase (i.e austenite, γ bainite, B or martensite, M).
λ	Thermal conductivity (W.m^{-1}. K^{-1})
ρ	Density (kg. m^{-3})
ϵ	Emissivity of oxidized steel
δ	Value criteria for the *MAPE* convergence

precise sequence of phase transformations from austenite to different products, such as martensite, bainite, pearlite or ferrite, depending on the steel composition. As a result, the phase mixture may vary from one point to another, and consequently, the mechanical properties of the material (Hardness, Yield and Ultimate Tensile Strength) are expected to vary from the surface to the core. High residual stresses are then generated in the block to balance the heterogeneity caused by the thermal gradient and non-uniform phase transformations. These stresses induce distortions that could even initiate cracks in severe cases [6,7]. It is therefore very important to understand and quantify the impact of various quenching parameters on the evolution of hardness, residual stresses and metallurgical structure [8].

Nevertheless, the traditional trial and error method is questionable, given the variability of the products (dimensions, steel composition, property requirements) and quenching conditions (austenitization temperature, quenching bath temperature, bath turbulence, positioning in the bath, etc.). Therefore, the quantification of quenching process parameters at industrial levels requires the development of reliable simulation tools that would integrate the coupling between thermal, metallurgical, and mechanical fields during the quench process [9].

The most important process parameter that influences the quench severity is the heat transfer coefficient (HTC), which estimates the heat extraction rate at the surface. An inaccurate estimation of HTC may lead to significant uncertainties in microstructure prediction or residual stress levels after quenching [9], due to the strong interactions between the temperature, microstructure, and mechanical properties. Similarly, an accurate determination of the material properties for each phase (i.e., austenite, bainite, martensite, etc.) at different temperatures is necessary, but very challenging and time consuming [10]. Generally, a constant HTC and material properties that are only temperature-dependent (i.e., that do not consider the influence of steel composition) are most commonly used [11–14]. HTC is often formulated as surface temperature-dependent in describing the wetting phases during water quenching (i.e., vapor blanket, boiling, convection) [15,16]. Although such simplifications may be reasonable when small parts are studied [17–20], their application to large size components may lead to significant inaccuracies in temperature prediction inside the block [10]. However, little data is available in the case of large size forged blocks, and most results that have been obtained are based on simulations with limited or no experimental validation during the quench process.

Several techniques and methods are used for HTC estimation during quenching. For instance, in small specimens, characterized by low Biot numbers ($Bi = \frac{hL}{\lambda} < 0.1$), it is usually assumed that the excitation due to the quench medium provides a uniform thermal field in the entire volume of the part (i.e., the surface and core react similarly) [15,21]. For this reason, the lumped capacitance model has been considered as a direct method for HTC calculation. The above assumption, however, is not applicable when quenching large size blocks which are characterized by non-uniform thermal fields. Attempts have been made to use a modified lumped capacitance method to estimate the HTC of large size shafts; however, significant differences between the experimental and simulated temperature profiles were observed [22].

Inverse thermal analysis has usually been considered as a suitable approach to determine HTC during cooling. In this procedure, the link between HTC and the calculated temperature could be established by several techniques such as finite difference, finite element or analytical methods. HTC is estimated indirectly during quenching by considering an optimization process in which the temperature cost function (sum of squared errors) between the calculated temperature and the measured one must be minimized [23]. However, the application of the inverse method in the determination of HTC in the case of cooling has been limited to medium size or axi-symmetrical 2D models, mostly due to the associated computational costs [20,24]. Publications on the application of 3D FEM combined with inverse methods in HTC determination are very limited, and often do not consider the effect of phase transformations [20,25,26].

In this investigation, a new methodology for the accurate determination of HTC during quenching of a large size steel block is presented. The methodology is based on the design of a progressive neural network between pre-existing HTC data and their corresponding calculated cooling curves using 3D FEM simulations in specific locations inside the block. A step-by-step approach was used to determine the most accurate estimation of HTC by minimizing errors between simulations and experimental measurements. The validity of the proposed model was assessed through the instrumentation of a large size ingot and temperature measurements during the quench process.

2. Coupled fields in numerical modeling of the quenching process

Steel quenching is a complex multi-physics problem during which, driven by heat transfer, phase transformations and mechanical interactions simultaneously takes place inside the material [27]. The occurrence of phase transformation in steel, from austenite to martensite, bainite, or pearlite, releases a significant amount of heat (latent heat) that must be taken into account [12]. However, the presence of significant thermal gradients during water quenching, particularly in the case of large size ingots, results in a variety of phase transformations (i.e., different amount of latent heats) at different locations of the ingot. Therefore, a metallurgical constitutive model is needed to predict the generated latent heat as an internal heat source during phase transformation. The final stress state of the part must therefore also incorporate the contribution from phase transformation in addition to that from the thermal gradient. Fig. 1 shows schematically the coupling between the temperature, stress and phase transformation that occurs during the steel quenching process.

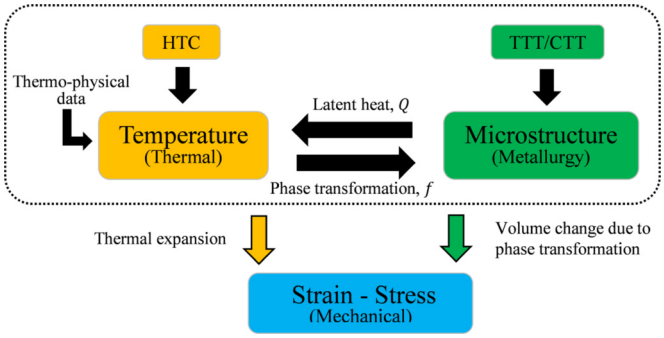

Fig. 1. Coupling between thermal, mechanical and microstructural fields in quench modeling.

The current quench problem was modeled by FEM using the quench module of Forge® NxT 1.1 software [28]. The code takes into account the coupling between thermal, metallurgical and mechanical phenomena, as described in Fig. 1. In the present study, only the coupling between the thermal and metallurgical fields were considered, as the focus of the paper is on the determination of an accurate HTC, and not on the generation of residual stresses. The constitutive equations used to solve thermal and phase transformation models are detailed in sections 2.1 and 2.2. It should be noted that the heat generation resulting from the plastic deformation due to quenching is not considered in the present numerical model due to its relatively minor effect on the overall heat balance of the large size ingot [27].

2.1. The thermal model

The thermal field could be modeled using the Fourier heat conduction equation of the transient problem as follows [29]:

$$\rho C_p \frac{\partial T}{\partial t} = div(\lambda \nabla T) + Q \tag{1}$$

with ρ,C_p and λ density being the specific heat and thermal conductivity, respectively, and where Q is the internal heat source due to the latent heat released after decomposition of the volume fraction of austenite (f_φ) to another φ-phase (φ represents austenite (γ), bainite (B) or martensite (M)).

This heat could be expressed as:

$$Q = \rho . \Delta H^\varphi . \dot{f}^\varphi = \rho . \Delta H^\varphi . \frac{df^\varphi}{dt} \tag{2}$$

The boundary conditions used for Eq. (1) are:

$$T(x, y, z, t = 0) = T(x, y, z); (x, y, z) \in \Omega \tag{3}$$

where

$T(x, y, z, t = 0)$ is the initial temperature of the block before quenching,

and

$$-\lambda \frac{\partial T}{\partial n} = q; (x, y, z) \in \Gamma \tag{4}$$

The term q is related to the heat transfer mechanism (e.g., convective, radiation) that governs the energy flow.

At the cooling stage, the total HTC describes the sum of the convective and radiative heat transfer coefficients at the surface of the workpiece [21]. Thus, Eq. (4) can be written as:

$$-\lambda \frac{\partial T}{\partial n} = HTC(T_s - T_f) = (h_c(T) + h_r(T))(T_s - T_f) \tag{5}$$

where

$$h_r(T) = \sigma . \epsilon . (T_s^2 + T_f^2)(T_s + T_f) \tag{6}$$

The HTC used in this study was applied on all the surfaces of the block as a boundary condition. Details regarding the HTC values are provided in sections 3.4 and 4.2, respectively. The emissivity of steel was set to $\epsilon = 0.8$, corresponding to an oxidized surface of a carbon steel during austenitization [1].

2.2. The phase transformation model

Water quenching of the large size steel block introduces a significant range of cooling rates between the surface and the core [30]. As a result, a gradient of microstructure from full martensite to full bainite is formed in the investigated large size forged ingots, as previously reported experimentally [31]. Thus, a thermo-physical property, P of the material, such as the thermal conductivity, density and specific heat during the quenching process, change as a function of the volume fraction, f^φ and the thermo-physical property, p^φ of each individual phase φ.

The additivity rule is generally used to quantify the contribution of each phase φ to different thermo-physical properties of the material at temperature T [32,33]:

$$P = \sum P^\varphi f^\varphi \tag{7}$$

In case of phase transformation under isothermal conditions, the calculation of the decomposed volume fraction of austenite is described by the John-Mehl-Avrami equation, considering the diffusion phenomenon [29]:

$$f = 1 - exp\{-\theta t^n\} \tag{8}$$

In the present analysis, the nucleation and growth of a new phase during quenching occurs under non-isothermal conditions. Phase transformation during continuous cooling was divided into the sum of a finite number of isothermal steps using the Scheil's additivity rule [34]:

$$\sum \frac{\Delta t}{\tau_i(T)} = 1 \tag{9}$$

Two variables, fictitious time, t_i^*, and fictitious volume fraction of transformed phase, f_i^*, were used to obtain the real transformed fraction of each phase. They are represented by the following equations:

$$t_i^* = \left[\frac{-\ln(1-f_{i-1})}{\theta_i}\right]^{1/n_i} \tag{10}$$

t_i^* represents the total time required at temperature T_i to form a volume fraction of the new phase equivalent to the summative quantities of the transformed phases until T_i.

The time interval, Δt, at each temperature step is:

$$t_i = \Delta t + t_i^* \tag{11}$$

Therefore,the amount of fictitious the transformed phase is given by:

$$f_i^* = 1 - exp\left\{-\theta_i\,(t_i^* + \Delta t)^{n_i}\right\} \tag{12}$$

Hence, the real transformed fraction at the end of each time step is defined by:

$$f_i = f_i^*\,(f_{i-1}^{\gamma} + f_{i-1})\,f_{max} \tag{13}$$

where f_{max} is the maximum possible amount of the new fraction, and f_{i-1}^{γ} and f_{i-1} are respectively the untransformed austenite and new phase transformed fraction at the time step $i-1$.

For martensitic transformation, the Koistinen-Marburger equation was employed in the numerical modeling as follows [29]:

$$f^M = 1 - exp\,\{-\alpha(T - M_s)\} \tag{14}$$

3. Material and methods

3.1. Experimental setup and procedures

The instrumentation of the forged block and the quench bath followed specific procedures to ensure that the experimental conditions are consistent with the simulation conditions, as described below:

3.1.1. Block Instrumentation

A large size block measuring 2566 × 1220 × 508 mm^3 was austenitized at 871 °C in a gas-fired furnace and then quenched and maintained in agitating water at 20 °C for 2.5 h. The forging and quenching processes were conducted at Finkl Steel-Sorel Forge, Sorel, Quebec, Canada. Cooling curves were obtained during the quenching process by embedding two K-type thermocouples (TC_1 & TC_2). The standard error associated to the thermocouples measurement in the experienced range of temperature was estimated to be ± 0.75%.

The chemical composition of the forged medium carbon low alloy steel ingot used in the present investigation was provided in Table 2.

Fig. 2 illustrates the size of the block and the positions of TC_1 and TC_2 and their corresponding sensors in the FEM model.

The data extracted from the thermocouples were implemented in the ANN model to predict HTC and study the effectiveness of the FEM simulation. Details regarding the progressive ANN will be presented in section 3.5.

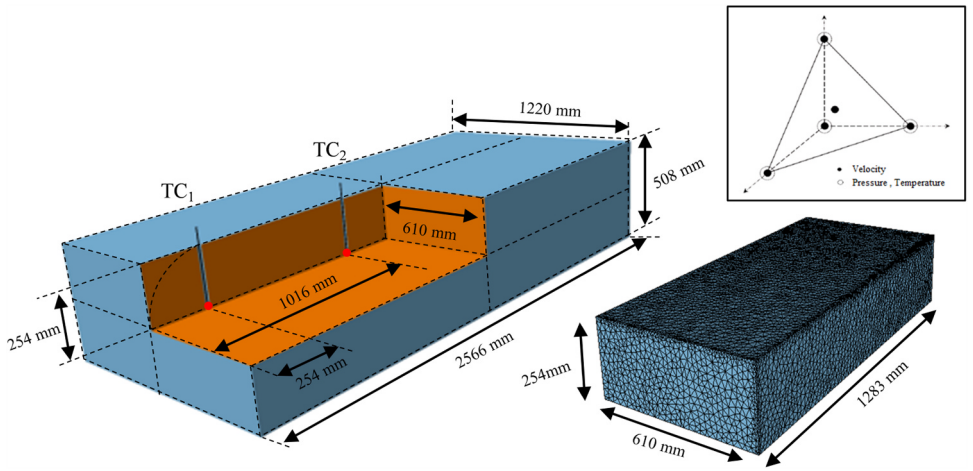

Fig. 2. Geometry of the quenched block, position of the thermocouples, meshing and the tetrahedral elements used for FEM simulation.

3.1.2. Quench bath Instrumentation

The quench bath was equipped with pumps to maintain constant water contact by providing high recirculation over the block (forced convection). To assess the interfacial heat transfer between the block and the quenchant, two supplementary thermocouples were used to record the evolution of the inlet and the outlet water temperatures in the quench bath. T_{Mean} was the average temperature between the inlet and outlet thermocouples, which was used as an input temperature, T_f in FEM simulations. Table 1 shows the evolution of the inlet, outlet and the calculated mean temperature, which represents the medium temperature.

Table 1
Evolution of the quench bath temperature during the process.

Time (s)	0	300	600	900	1200	1800	3300	4500	5700	7200	9300
T_{Inlet} (°C)	20	20	20	20	20	20	20	20	20	20	20
T_{Outlet} (°C)	38.4	46.8	49.7	50.8	51.0	50.1	44.9	39.8	36.0	34.2	32.6
$T_{Mean} = T_f$ (°C)	29.2	33.4	34.8	35.4	35.5	35.0	32.4	29.9	28.0	27.1	26.3

3.2. Material data set

3.2.1. TTT/CCT diagrams

Time-Temperature-Transformation (TTT) and Continuous-Cooling-Transformation (CCT) diagrams provide critical information with regard to phase transformation occurring under isothermal (TTT) or non-isothermal (CCT) conditions [30] which are used as input data in the simulation of the quenching process [35–37]. In the present investigation, JMatPro® software [33] was utilized for the generation of the TTT and CCT diagrams of the investigated steel. It should be noted that such an approach has successfully been used in the case of highly alloyed steel [38]. However, for further validation, the predicted CCT diagram was compared with the one previously determined experimentally by some of the authors in this work [39], and the results are reported in Fig. 3.

It can be seen that there is good agreement, particularly for B_S and M_S between the experimentally observed CCT diagram and the calculated one. The above comparison confirms the reliability of the calculated TTT by JMatPro®, which will be used as input for the FEM analysis.

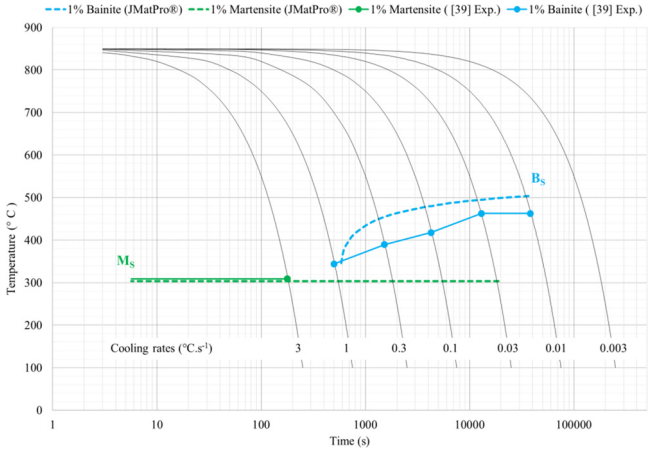

Fig. 3. Comparison between experimental CCT determined from [39] and the simulated one using JMatPro®.

Table 2
Typical chemical analysis of the investigated steel - % weight.

C	Mn	Si	Ni	Cr	Mo	Other
0.33	1.00	0.40	0.50	1.85	0.50	Micro-alloying

3.2.2. Thermo-physical properties

A combination of data from the literature and JMatPro® was also used for estimating the thermo-physical properties. This approach has already been used by several other authors [33,40,41], and is considered accurate enough over the temperature range of interest that covers the quench process, especially for thermal conductivity $\lambda(T)$, specific heat $C_p(T)$ and density $\rho(T)$. The latent heat released during martensitic transformation was also calculated by JMatPro®, and considered equal to that corresponding to bainitic transformation ($\Delta H^B = \Delta H^M$) based on Piekarska's studies [42,43].

3.3. FEM model specifications

Initially, the 3D model of the workpiece was built using Catia V5R21 software. The symmetrical shape of the block allowed the use of one eighth (1/8) of the model. The model was then imported into Forge® NxT 1.1 code for meshing. The P1 + /P1 linear tetrahedral mesh elements with four integration points, for the temperature-pressure was implemented to discretize the 3D model. The independence of the grid was tested by varying progressively the grid size until reaching an optimized number of nodes (18,210) and elements (86,664) that ensure both precision and convergence in an acceptable calculation time. Fig. 2 shows the 3D FEM model and the mesh type used for the simulations. It should be noted that the time step during the FEM simulations was controlled automatically by the software using implicit schemes (Crank Nicolson's scheme for initialization, followed by Dupont's scheme) [34]. The above approaches allowed a better stability of the calculation and reduced the impact of temperature oscillations due to thermal shock during quenching, as detailed in [34,44].

Table 3 below summarizes all the inputs used for FEM simulations.

Table 3
FEM Simulation input parameters.

Material parameters	Process parameters
TTT/CCT: Acquired from JMatPro® (Calibrated with experimental data in Fig. 3) Thermo-physical properties: $\rho(T)$, $\lambda(T)$, $C_p(T)$ (JMatPro®) Latent heat (JMatPro®) $\Delta H^B = \Delta H^M$ The emissivity of steel: $\epsilon = 0.8$	Geometry: 2566 × 1220 × 508 mm^3 using one-eighth (1/8) symmetrical model (Fig. 2) Initial temperature = 871 °C (Austenitization temperature) The medium temperature: averaged from experimental measurement (Table 1) HTC^{1-5}: acquired from the literature (Fig. 4(b)) $HTC^{ANN_{1-6}}$: acquired from ANN predictions (Fig. 6)

3.4. Neural network specifications

In order to optimize the HTC parameter related to the quenching process of the large size steel block, an ANN approach was implemented under MATLAB using the Neural Network ToolBox [45]. The structure of the network, the activation function and the learning algorithm are the main requirements which should be implemented in an ANN.

The output data of the ANN were digitized from five HTC profiles reported in the literature in the works of Li, H. et al. (2008) on quenching of a steel similar to that investigated in the present study [20]. As shown in Fig. 4(b), the data were chosen, to cover the largest possible range of HTC fluctuations in order to allow a better training of the data, thereby increasing the accuracy and reliability of the predictions.

On the other hand, each HTC pattern was introduced as a boundary condition in the FEM code to calculate the temperature evolution for each 300 s time interval during the total quenching time (9300 s) of the block. In particular, the temperature profile T_i at TC_1 for each time step was considered as an input for the ANN (Fig. 4(a)).

To present the dimensionless temperature and heat transfer coefficient, the input and the output samples were automatically normalized by MATLAB between -1 and 1 using the following equations:

$$T_n = \frac{2(T - T_{min})}{(T_{max} - T_{min})} - 1 \tag{15}$$

$$HTC_n = \frac{2(HTC - HTC_{min})}{(HTC_{max} - HTC_{min})} - 1 \tag{16}$$

A back-propagation (BP) learning algorithm, between HTC_k data and T_i data simulated by FEM at TC_1, was selected for data training, as can be seen in Fig. 4(c). One hidden layer was set in ANN architecture with eight neurons, which, after several trials, proved to be efficient for training.

The weights w_{ji}, w_{kj} and the bias b_j, b_k of the neural network indicate how the network alters the association of the neurons.

At the level of the hidden layer, the above variables generate a trigger value u_j toward the node j [46], using the following equation:

$$u_j = \sum_{i=1}^{N} w_{ji}.\ T_i + b_j \tag{17}$$

In this work, the use of the hyperbolic tangent as an activation function for hidden and output layers provided better performances. The “tansig” transfer function at the output of the hidden layer is given by:

$$a(u_j) = \frac{e^{u_j} - e^{-u_j}}{e^{u_j} + e^{-u_j}} \tag{18}$$

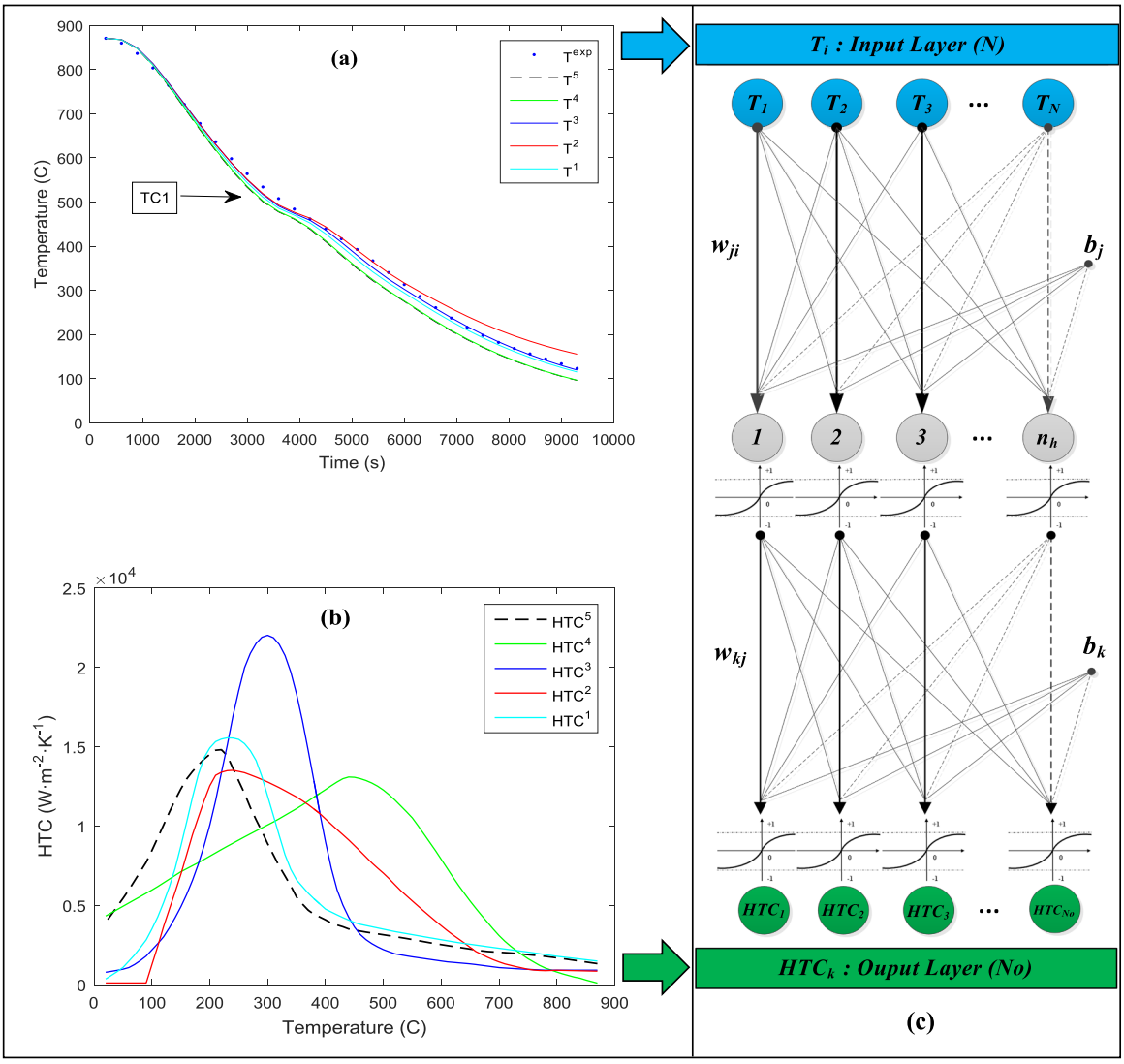

Fig. 4. (a) Predicted cooling curves (solid lines) obtained by FEM using HTC^{1-5} and experimental temperature profile (dotted lines) recorded by the thermocouple located in the near surface (TC_1). (b) HTCs digitalized from the works of [20] used as output for ANN training. (c) Schematic of the back-propagation ANN training used in the present study.

The activation function is also applied to each node of the output layer by the following equation:

$$HTC_k = a\left(\sum_{j=1}^{n_h} w_{kj}.\ a(u_j)+b_k\right) \tag{19}$$

The Levenberg-Marquardt algorithm (TRAINLM), which is known to be a fast converging algorithm and one that has already been used for calculating HTC, was selected for [47,48] training. The training of the ANN network was considered efficient when a correlation coefficient above 0.95 was obtained ($R \geq 0.95$). A script was written in MATLAB, in order to maintain an automatic training until the required value of R was achieved.

The correlation coefficient during training, validation and testing was defined as follows:

$$R = \frac{\sum_1^{N_o}\left(HTC_k^{target}-\overline{HTC_k^{target}}\right)\sum_1^{N_o}\left(HTC_k^{output}-\overline{HTC_k^{output}}\right)}{\sqrt{\sum_1^{N_o}\left(HTC_k^{target}\right)^2.\ \sum_1^{N_o}\left(HTC_k^{output}\right)^2}} \tag{20}$$

The experimental cooling temperature T^{exp} recorded at TC_1 was used for the simulation of the network after being trained. HTC^{ANN_p} denotes the predicted HTC using ANN simulations, where p represents the number of predictions. The HTC^{ANN_p} was then smoothed with MATLAB to adjust the prediction irregularities at certain temperature zones before having it added to the previous

trained network.

The effectiveness of prediction due to any HTC^x was indirectly evaluated by using the mean absolute percentage error (*MAPE*) between the T^{exp} and its corresponding T^x. The *MAPE* for any calculated T^x is expressed as:

$$MAPE = \frac{1}{N}\sum_{i=1}^{N}\left|\frac{T_i^{exp} - T_i^x}{T_i^{exp}}\right| = \frac{1}{N}\sum_{i=1}^{N} e_i \tag{21}$$

where e_i is the absolute percentage error between T_i^{exp} and T_i^x for each time step i, with $\Delta t_i = 30\,0\,s$. The coefficient N is the same as defined in Fig. 4(c).

3.5. Configuration of the ANN with FEM model for HTC optimization

The five selected HTC^{1-5} and their corresponding FEM simulations T^{1-5} at TC_1 sensor was used for the initialization of the ANN in MATLAB (left block in the flow chart of Fig. 5). Specifically, the matrices $[T]_{i\times m}$ and $[HTC]_{k\times m}$ (with m = 5) were used as input and output layers of the proposed ANN model (*ANN Training BLOCK* in the flow chart of Fig. 5), respectively.

Once the ANN training is completed, the ANN simulation step takes place using the experimental temperature, T^{exp}, as input (the *ANN Simulation BLOCK* in the flow chart of Fig. 5). The HTC predictions based on ANN simulations are only considered acceptable

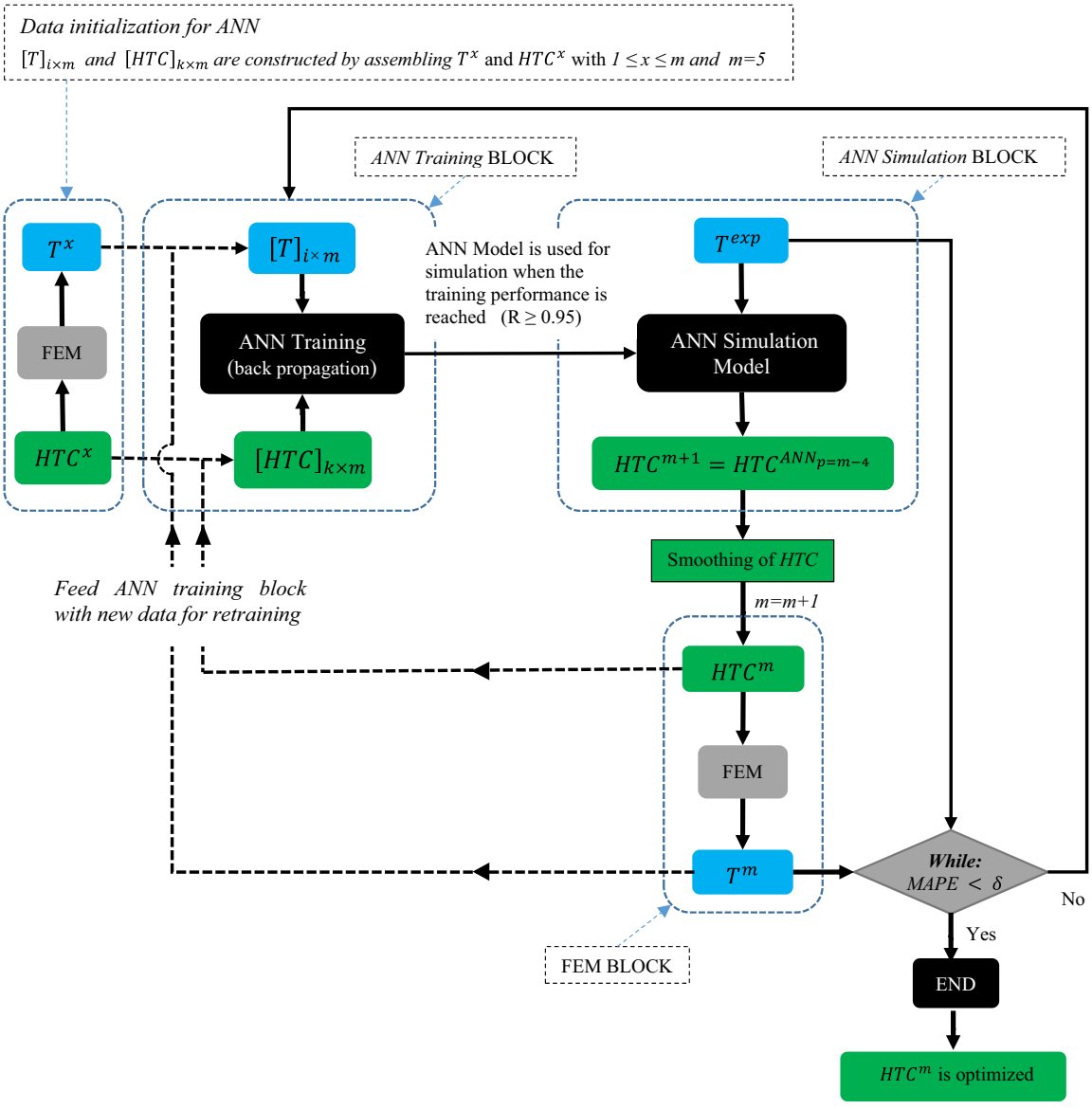

Fig. 5. Flow chart of HTC prediction using ANN combined with FEM.

when the *MAPE* is smaller than the minimum specified value, δ. As long as the *MAPE* does not meet the specified criteria, both the predicted HTC^{ANN_p} (ANN simulations) and T^{ANN_p} (FEM simulations) are added simultaneously to the previous network dataset for retraining. After each prediction, the network grows progressively by feeding the input matrix $[T]_{i\times m}$ and the output matrix $[HTC]_{k\times m}$ respectively with new columns T^{ANN_p} and HTC^{ANN_p} to transform the new dataset to $[T]_{i\times m+1}$ and $[HTC]_{k\times m+1}$ for a new training. The flow chart used for HTC prediction is illustrated in Fig. 5.

The ANN_p notation is used mainly to distinguish between the predicted and the initially trained HTC drawn from the literature; nevertheless, the two categories could be linked as follows: $(HTC^{ANN_1} = HTC^6, HTC^{ANN_2} = HTC^7 ...)$

The ranking of the HTC^{ANN_p} accuracy is managed mainly by *MAPE* minimization, with the tracking of the maximum error $Max\,(e_i)$ indicating the magnitude and the location of the errors.

4. Results and discussion

4.1. ANN predicted HTC Profile

For each prediction of HTC^{ANN_p}, obtained using ANN simulation, the performance of the trained network was tested using the correlation coefficient '*R*'. The initial datasets were limited (5 HTC profiles) and dispersed (differences in HTC profiles), which made it difficult to identify the patterns between data from the first two trained networks (under fitting). However, after the third training, the progressing ANN showed excellent performance. Fig. 6 shows that the first two predicted HTC^{ANN_1} and HTC^{ANN_2} present different shapes from HTC^{1-5} used for the initial training. It should be noted that starting from the third prediction, the shape of HTC^{ANN_3} is converging for a common shape like as indicated for HTC^{ANN_4}, HTC^{ANN_5} and HTC^{ANN_6}, with the maximum HTC value being located at around 320 °C.

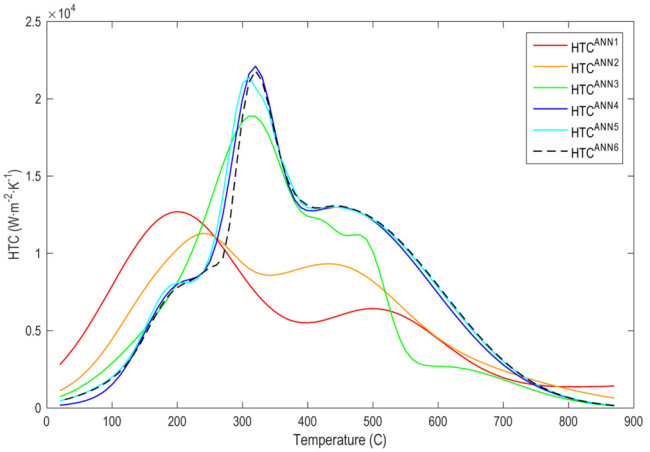

Fig. 6. HTCs predicted by ANN.

4.2. Temperature prediction using HTCs predicted via ANN

As it can be seen in Fig. 7, the temperature values of the cooling curves at TC_1 are lower than those at TC_2. This is related to the position of TC_1 which is located at a shorter distance from the cooled surfaces of the block as compared to TC_2, which is located in the center region of the block (see Fig. 2). The center region is only affected by the cooling of the top and bottom surfaces (assumption of an infinite rectangular parallelepiped) as a consequence of the thermal inertia due to the large length (2.56 m) of the block, as opposed to TC_1, which is affected by several surfaces. Accordingly, the *MAPE* was evaluated at the level of TC_1 to cover and average the effect of convection for all surfaces of the block. Fig. 7 also shows that the cooling curves, $T^{ANN_{1\text{-}6}}$, calculated using $HTC^{ANN_{1\text{-}6}}$ get progressively closer to the target temperature, T^{exp}, especially for T^{ANN_5} and T^{ANN_6}, which show the best fits.

Further analysis of Fig. 7 indicated that, both experimental and simulated cooling profiles show a change in the slope at around bainite start temperature, *Bs*; however, the change is more significant for TC_2 thermocouple. This change is mostly related to the latent heat generated as a result of bainitic transformation. The larger difference observed for TC_2 is due to the higher transformed proportion of bainite (i.e. higher heat generation) in the center compared to the near-surface region where TC_1 is located. The large size of the block is another contributing factor to a higher temperature increase at the center, as the generated heat will take longer to be evacuated compared to the surface regions. It must be noted that accurate estimation of the latent heat of transformation has been a challenge for scientists and sometimes important differences between the predicted and measured values are reported as in the works of [22,49].

In the present work, the latent heat value obtained from the database of the JMatPro® software appears to be overestimated. An Attempt was made to use the assumption considered by Piekarska [42,43] to improve latent heat prediction; however, the over-estimation for TC_2 was still visible, as indicated in Fig. 7. A comprehensive experimental study is needed to accurately estimate the

latent heat of phase transformation during cooling and will further increase the quality of the predictions; however, such study was not in the scope of the present investigation.

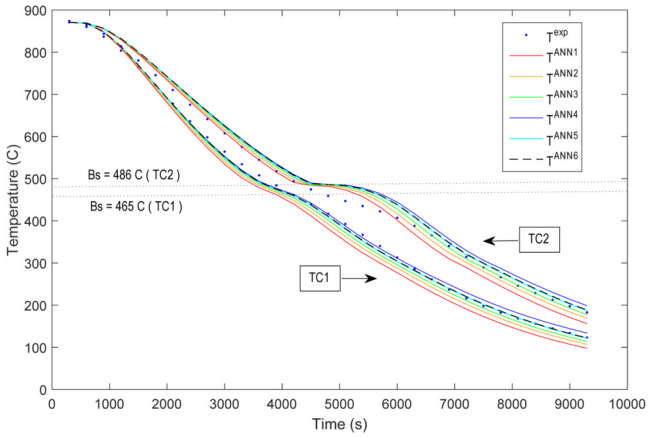

Fig. 7. FEM of cooling curves using predicted HTCs.

4.3. Prediction accuracy and error analysis

The analysis of the prediction effectiveness based on the predicted HTCs in Table 4 indicates that both the *MAPE* and the maximum error were improved after each ANN simulation (i.e. after each prediction). T^{ANN_6} presents the best performance for all predictions, with a *MAPE* value of 1.47% and a maximum error of 3.78%. Accordingly, it can be said that HTC^{ANN_5} and HTC^{ANN_6} perform almost equally. However, it can be seen that the *MAPE* improved by only 0.08% from T^{ANN_5} to T^{ANN_6}, indicating that the maximum effectiveness of prediction was already reached by HTC^{ANN_5}. Moreover, as shown in Table 4, because after HTC^{ANN_5} it is difficult to further reduce the error (*MAPE* reducing from 1.55% to 1.47%); therefore HTC^{ANN_6} could be considered as redundant. This over-fitting explains why the subsequent training predicts the same common shape, with only minor differences.

The character of the predicted datasets via ANN are supposed to cover the "unknown" real HTC curve of the studied quench process, with less dispersion (*MAPE* < 10%). Feeding the ANN with that kind of data increases the quality of the datasets and helps to make the network training process easier [49].

It must be noted that the accuracy of the predictions is also intimately dependent on the quality of the experimental inputs (T^{exp}). Generally, during quenching of large steel components, factors related to the material inhomogeneity and/or the instrumentation process itself, may affect the uncertainty of the experimental measurements. For example; a local change in chemical composition, due to the occurrence of macro-segregation, may affect the metallurgical field [50] and therefore result in slight deviations in the thermal field. Considering the large size of the component, obtaining the precise location of the thermocouples in deep drilled holes or an estimation of the disturbance of the thermal field introduced by drilled cavities [51] are challenges that cannot be easily overcome from a technical point of view. Such uncertainties may also play a role in the differences observed between the experimental measurements and simulation results.

Table 4
Analysis of FEM effectiveness using the predicted $HTC^{ANN_{1\text{-}6}}$.

	e^{ANN_1}	e^{ANN_2}	e^{ANN_3}	e^{ANN_4}	e^{ANN_5}	e^{ANN_6}
Max (e_i)	20.57%	13.13%	7.74%	8.69%	4.12%	3.78%
MAPE	8.53%	5.56%	3.36%	2.97%	1.55%	1.47%

5. Conclusions

The following conclusion can be drawn from the present study:

1) A new approach using a combination of a progressive ANN and FEM was used to improve HTC prediction in the water quench process of large size forged steel blocks. Experimental measurements, by instrumentation of the large size blocks, were carried out to provide data for the ANN, as well as to validate FEM results.
2) The shape of the $HTC^{ANN_{4\text{-}6}}$ predicted by ANN (including HTCs with less than 3.0% *MAPE*) shows the establishment of a recurrent pattern that is similar in the water quench field, and it could be described by the wetting kinetics process during water quenching.
3) The minimum average deviation between the experimental and FEM-calculated temperature was 1.47%, indicating that the optimal HTC was predicted. It is believed that the progressive ANN increased step by step the quality of data preparation for the coming trainings, which improves significantly the accuracy of prediction in this study.

Acknowledgments

This project was carried out in collaboration with Finkl steel-Sorel through a MITACS IT03151 Grant whose support is acknowledged. The authors are also very grateful to Finkl Steel, especially the R&D and Engineering Departments, for providing the large size block, as well as the instrumentation and measurements used in the present research.

References

[1] ASM International Handbook Committee, ASM Handbook , Heat Treating, ASM International, 1991.
[2] O. Jaouen, F. Costes, A. Saad, P. Lasne, R. Ducloux, Advanced solutions for virtual process modelling: application to steel ingot manufacturing from casting to open-die forging, Proceedings of the 16th International Conference Metal Forming 2016, 2016.
[3] G.E. Totten, Heat-Treating Process Design, Handbook of Metallurgical Process Design, CRC Press, 2006.
[4] F. Beaudet, C. Blais, H. Lehuy, B. Voyzelle, G. L'espérance, J.-P. Masse, M. Krishnadev, Improvement of hardenability and static mechanical properties of P20+0.5 Ni mold steel through additions of vanadium and boron, ISIJ Int. 52 (3) (2012) 424–433.
[5] K. Araki, T. Yuasa, Y.-.T. Tamura, Heat-Treated Steel Plates with Heavy Section and Large Product Weight, JFE technical report, 2013.
[6] L. Cheng, Z. Liwen, Qa Zhang, Z. Quying, W. Zhaokun, Numerical simulation and technological parameter optimization for quenching process of a gas turbine compressor disk based on Metallo-Thermo-mechanics, J. Mater. Sci. Technol. 22 (06) (2006) 860–864.
[7] G.Y. Liu, L.M. Dong, K.K. Wang, D.M. Zhu, S.J. Zhang, S.C. Gong, M.W. Li, Water–air online quenching process of 3Cr2Mo steel based on numerical simulation, Ironmak. Steelmak. 43 (10) (2016) 780–789.
[8] C. Totten, M. Narazaki, R. Blackwood, L. Jarvis, Failures related to heat treating operations (ASM Handbook Committee)(Ed.)(, Failure Analysis and Prevention), ASM International, 2002, pp. 192–226 (ASM Handbook Committee)(Ed.)(, Failure Analysis and Prevention).
[9] C. Şİmşİr, A Mathematical framework for simulation of thermal processing of materials: application to steel quenching, Turk. J. Eng. Environ. Sci. (2008) 85–100.
[10] G.E. Evcil, O. Mustak, C. Simsir, Simulation of through-hardening of SAE 52100 steel bearings – Part II: validation at industrial scale, Mater. und Werkst. 47 (8) (2016) 746–754.
[11] H.K.D.H. Bhadeshia, Bainite in Steels: transformations, Microstructure and Properties, IOM Communications, 2001.
[12] K. Perzynski, L. Madej, A. Szajding, K. Raga, K. Kubiak, A. Niechajowicz, K. Jaskiewicz, Z. Gronostajski, M. Pietrzyk, Numerical evaluation of gear ring behavior during various cooling conditions, J. Mach. Eng. 16 (2) (2016) 18–26.
[13] M. Jung, M. Kang, Y.-K. Lee, Finite-element simulation of quenching incorporating improved transformation kinetics in a plain medium-carbon steel, Acta Mater. 60 (2) (2012) 525–536.
[14] W. Porto de Oliveira, M. Savi, P. Pacheco, L. Souza, Thermomechanical analysis of steel cylinders quenching using a constitutive model with diffusional and non-diffusional phase transformations, Mech. Mater. 42 (1) (2010) 31–43.
[15] H.S. Hasan, M.J. Peet, J.M. Jalil, H.K.D.H. Bhadeshia, Heat transfer coefficients during quenching of steels, Heat. Mass Transf. 47 (3) (2011) 315–321.
[16] A.S. Hans, M. Tensi, George E. Totten, Quenching and Quenching Technology, Steel Heat Treatment, CRC Press, 2006.
[17] S. Singer, Sensitivity of the heat-transfer coefficient calculation, Mater. Perform. Charact. 3 (4) (2014) 184–209.
[18] B.L. Ferguson, Z. Li, A.M. Freborg, Characterizing water quenching systems with a quench probe, J. Mater. Eng. Perform. 23 (12) (2014) 4197–4201.
[19] A. Sugianto, M. Narazaki, M. Kogawara, A. Shirayori, A comparative study on determination method of heat transfer coefficient using inverse heat transfer and iterative modification, J. Mater. Process. Technol. 209 (10) (2009) 4627–4632.
[20] H. Li, G. Zhao, L. He, Y. Mu, High-speed data acquisition of the cooling curves and evaluation of heat transfer coefficient in quenching process, Measurement 41 (6) (2008) 676–686.
[21] Y.A. Cengel, Heat Transfer: A Practical Approach 2nd Edition, 2002.
[22] M. Boniardi, M. Guagliano, A. Casaroli, R. Andreotti, F. Ballerini, Large Forgings: Microstructural evolution and residual stresses due to quenching treatments—A combined Numerical and Experimental approach, Mater. Perform. Charact. 3 (4) (2014) 118–136.
[23] L. Wood R, The design of experiments for inverse thermal analysis, Proc. Inst. Mech. Eng. Part B. J. Eng. Manuf. 220 (2) (2006) 225–241.
[24] I. Felde, S. Szénási, A. Kenéz, S. Wei, R. Colas, Determination of complex thermal boundary conditions using a Particle Swarm Optimization method, Proceedings of the 5th International Conference on Distortion Engineering, 2015, pp. 227–236.
[25] L. Huiping, Z. Guoqun, N. Shanting, L. Yiguo, Inverse heat conduction analysis of quenching process using finite-element and optimization method, Finite Elem. Anal. Des. 42 (12) (2006) 1087–1096.
[26] Z. Malinowski, T. Telejko, B. Hadała, A. Cebo-Rudnicka, A. Szajding, Dedicated three dimensional numerical models for the inverse determination of the heat flux and heat transfer coefficient distributions over the metal plate surface cooled by water, Int. J. Heat. Mass Transf. 75 (Supplement C) (2014) 347–361.
[27] C. Şimşir, C.H. Gür, A simulation of the quenching process for Predicting temperature, microstructure and residual stresses, Stroj. Vestn./J. Mech. Eng. 56 (2) (2010).
[28] FORGE®NxT, ⟨http://www.transvalor.com/en/cmspages/traitement-thermique.62.html.)⟩.
[29] C. Şİmşİr, 3D Finite Element Simulation Of Steel Quenching In Order To Determine The Microstructure And Residual Stresses, The Graduate School Of Natural And Applied Sciences, Middle East Technical University, 2008.
[30] B. Liščić, Steel Heat Treatment, Steel Heat Treatment, CRC Press, 2006.
[31] D.L. Song, J.F. Gu, J.S. Pan, M.J. Hu, Numerical simulation of quenching of large sized blocks of 718 steel used for plastic dies, Mater. Sci. Technol. 20 (12) (2004) 1567–1572.
[32] S.H. Kang, Y.T. Im, Thermo-elasto-plastic finite element analysis of quenching process of carbon steel, J. Mater. Process. Technol. 192–193 (2007) 381–390.
[33] N. Saunders, U.K.Z. Guo, X. Li, A.P. Miodownik, J.P. Schillé, Using JMatPro to model materials properties and behavior, JOM 55 (12) (2003) 60–65.

[34] D. Cardinaux, Étude et modélisation numérique 3D par éléments finis d'un procédé de traitement thermique de tôles embouties après chauffage par induction: application a un renfort de pied central automobile, Éc. Dr. 364: Sci. Fondam. Et. Appliquées, Éc. Natl. Supér. Des. Mines De. Paris (2008).
[35] P.-z. Cao, G.-z. Liu, K. Wu, Study of heat treatment parameters for large-scale hydraulic steel gate track, Water Sci. Eng. 6 (4) (2013) 423–432.
[36] B. Smoljan, S. Smokvina, Hanza, N. Tomašić, D. Iljkić, Computer simulation of microstructure transformation in heat treatment processes, J. Achiev. Mater. Manuf. Eng. 24 (1) (2007).
[37] B. Buchmayr, J.S. Kirkaldy, Modeling of the temperature field, transformation behavior, hardness and mechanical response of low alloy steels during cooling from the austenite region, J. Heat. Treat. 8 (2) (1990) 127–136.
[38] J.-P. Schillé, Z. Guo, N. Saunders, A.P. Miodownik, Modeling phase transformations and material properties critical to processing simulation of steels, Mater. Manuf. Process. 26 (1) (2011) 137–143.
[39] S.M. Chentouf, M. Jahazi, L.-P. Lapierre-Boire, S. Godin, Characteristics of austenite transformation during post forge cooling of large-size high strength steel ingots, Metallogr., Microstruct., Anal. 3 (4) (2014) 281–297.
[40] O. Mustak, E. Evcil, C. Simsir, Simulation of through-hardening of SAE 52100 steel bearings – Part I: determination of material properties, Mater. und Werkst. 47 (8) (2016) 735–745.
[41] Z. Guo, N. Saunders, J.P. Schillé, A.P. Miodownik, Material properties for process simulation, Mater. Sci. Eng.: A 499 (1–2) (2009) 7–13.
[42] W. Piekarska, M. Kubiak, Theoretical investigations into heat transfer in laser-welded steel sheets, J. Therm. Anal. Calorim. 110 (1) (2012) 159–166.
[43] W. Piekarska, Modelling and analysis of phase transformations and stresses in laser welding process / modelowanie I analiza przemian fazowych I Naprężeń W procesie spawania laserowego, Arch. Metall. Mater. 60 (4) (2015) 2833.
[44] C. Aliaga, Simulation numérique par élément finis en 3D du comportement thermomécanique au cours du traitement thermique d'aciers: application a la trempe de pieces forgées ou coulées, Ecole Nationale Supérieure des Mines de Paris, 2000.
[45] M.H. Beale, M.T. Hagan, H.B. Demuth, Neural Network Toolbox™ User's Guide, The Mathworks Inc, 1992.
[46] S. Azizi, E. Ahmadloo, Prediction of heat transfer coefficient during condensation of R134a in inclined tubes using artificial neural network, Appl. Therm. Eng. 106 (2016) 203–210.
[47] R. Soundararajan, A. Ramesh, S. Sivasankaran, A. Sathishkumar, Modeling and analysis of mechanical properties of aluminium alloy (A413) processed through squeeze casting route using artificial neural network model and statistical technique, Adv. Mater. Sci. Eng. (2015 () (2015).
[48] M. Ilker, H.T. ARAT, Prediction Of heat transfer coefficients By Ann For aluminum and steel material, Int. J. Sci. Knowl. 5 (2014).
[49] B.D. Klein, D.F. Rossin, Data quality in neural network models: effect of error rate and magnitude of error on predictive accuracy, Omega 27 (5) (1999) 569–582.
[50] M. Hunkel, D. Nadolski, Coupled process simulation of cold extrusion and heat treatment distortion of steel shafts, Mater. und Werkst. 47 (8) (2016) 762–770.
[51] D.I. Li, M.A. Wells, Effect of subsurface thermocouple installation on the discrepancy of the measured thermal history and predicted surface heat flux during a quench operation, Metall. Mater. Trans. B 36 (3) (2005) 343–354.